Journal of Geophysical Research – Planets

Supporting Information for

Widespread Megaripple Activity Across the North Polar Ergs of Mars

Matthew Chojnacki[*1] (mchojnacki@psi.edu), David A. Vaz[2], Simone Silvestro[3,4], and & David C.A. Silva[2].

[1]Planetary Science Institute, Lakewood, CO, USA., [2]Centre for Earth and Space Research of the University of Coimbra, Observatório Geofísico e Astronómico da Universidade de Coimbra, Coimbra, Portugal. [3]SETI Institute, Carl Sagan Center, Mountain View, CA, USA. [4]INAF Osservatorio Astronomico di Capodimonte, Napoli, Italia. *Corresponding Author

Contents of this file

Introduction

Supplementary materials include a detailed methodology for the derivation of dune topography (**Section 1)** and change detection (**Section 2**). Additionally it includes tables with information for study sites (**Table S1**) and Objective 1 survey results (**Table S2**). Six supplementary figures provide additional context and details for our analysis.

Included animations provide additional evidence for bedform activity or inactivity. Animations 1-2, 4, and 6-8 were built using in-house software, which takes orthophoto subsets, stacks them in chronological order, and provides relevant context information such as Mars date (Mars year, L_s), the direction of north, and solar azimuth. As per convention, the solar longitude (L_s) range of 0°–360° defines a MY and 11 April 1955 (L_s =0°) is the start of the Mars calendar at MY01 (see *Piqueux et al.* (2015) for details). Other animations were generated from manually triangulated orthoimage subsets (see **Table S1**), and constructed in Photoshop. Compare with similar animated GIFs of non-polar migrating dunes and megaripples at http://www.uahirise.org/sim/ and some of our earlier work (Chojnacki et al., 2019; Silvestro et al., 2020).

Section 1. Derivation of dune topography and change detection

To quantify dune heights and movement, high-resolution topography and orthoimages were derived using stereo photogrammetry via SOCET SET® BAE system software (see Kirk et al., 2008). The resulting DTMs possess a horizontal post spacing of 1 meter, where the quality of pixel matching is provided by SOCET SET as a RMS error that is typically 0.3–0.7 of the HiRISE pixel scale (i.e., 25 cm) (Kirk et al., 2008; Sutton et al., 2015) and are reported in those Planetary Data Systems products (available at: https://www.uahirise.org/dtm/). These HiRISE Digital Terrain Models (DTMs) were registered to Mars Orbiter Laser Altimeter (MOLA) (Smith et al., 2001) shot points for absolute elevation. DTMs generally possess a vertical precision of ~30 cm based on the convergence angle and spatial resolution of the stereo pair (Kirk et al., 2003) and can resolve small topography such as megaripples (e.g., **Fig. S3**). Terrain artifacts generated during the photogrammetric terrain generation due to bland or deeply shadowed areas were recognized and avoided in co-registered HiRISE Figure of Merit (FOM) maps (Mattson et al., 2012). Stereo and monitoring images were then orthorectified to the DTM to allow change detection and bedform displacement quantification to be made. In some cases more recent HiRISE images were added to preexisting DTM projects (using the same quality standards) to extend the temporal coverage. DTMs available at: https://www.uahirise.org/dtm/

Section 2. Bedform sand flux calculations

Objective 3's quantification of whole dune field fluxes required multiple approaches applied to an Olympia Cavi reentrant aeolian site (232.9°E; 84.0°N). Dune slipface toe lines were mapped in QGIS at two different times (T1 and T2). These are used to derive migration vectors (m/Earth-year), assuming local bi-orthogonal trend along the lines. The heigh of the slipface is computed automatically, by sampling the image albedo and elevation along profiles which extend from the migration vectors. These two parameters are combined to allow the automatic mapping of the slipface brink points (see Fig. 3 in Urso et al. (2018)). With this procedure we estimate the volume of mobilized sediment, quantifying the fluxes ($m^3\ m^{-1}\ yr^{-1}$) continuously along the slipface. Flux uncertainties are estimated through error propagation, assuming 0.5 m of uncertainty for the displacements and slipface heights.

Many previous studies focused on barchan and barchanoid dunes, mapping dune advancement and crest height at the perceived center of the slipfaces (Bridges et al., 2011; Runyon et al., 2017; Chojnacki et al., 2017, 2019; Davis et al., 2020). Sediment fluxes were calculated multiplying the migration rate by dune height (Ould Ahmedou et al., 2007). Note that in this case, the computed fluxes correspond to discrete maximum fluxes (at the tallest section of the dune) and a likely overestimation. Instead, with the method used in this work we obtain a continuous averaged representation of the fluxes, which is more independent of the type and shape of the dunes. Thus, the adopted technique produces a more detailed representation of the avalanching fluxes, even when complex or compound slipfaces are analyzed.

Caution should be taken when comparing the results of the two methods, since fluxes can differ by one order of magnitude. Instead of reporting peak fluxes (multiplying the

maximum height by the average migration, like in Urso et al. (2018)) we compute mean and median fluxes by multiplying the two variable parameters along the slipfaces. This generates lower average fluxes, yet it is a more accurate representation of the overall fluxes (the same approach was followed in the flux comparison presented by Silvestro et al. (2020). For example, at Nili Fossae Chojnacki et al. (2018) derived 7.2 ± 3.9 $m^3 m^{-1} yr^{-1}$ for whole dune fluxes (HiRISE over 5 MY) whereas Silvestro et al. (2020) derived 3.4 ± 2.2 $m^3 m^{-1} yr^{-1}$ (HiRISE over the same time period) using this technique.

Ripple and megaripple displacements were quantified for the Buzzel site using COSI-Corr. HiRISE orthoimages can present small misalignments between the CCD channels as well as long-wavelength geometric distortions caused by jitter. These will generate residual displacements that can be filtered and subtracted from COSI-Corr EW and NS displacement components (**Fig. S6**). We applied the same technique used in Silvestro et al. (2020), which applies low-pass filtering to the residual components in the bedrock areas (assuming that displacements are zero) and extrapolating the residual values to dune areas using an inpainting algorithm. The average magnitude of the residuals is low (0.3±0.1 m for the example in **Fig. S6**), attesting the accuracy of the measured displacements.

Supplemental Figures

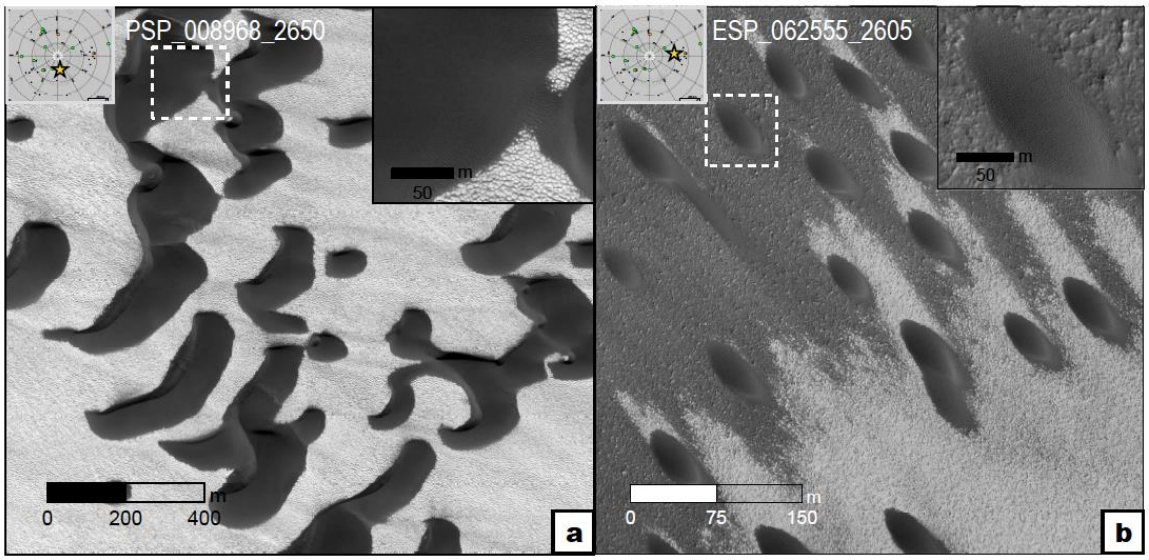

Figure S1. Two erg locations of highly active DTRs and dunes that lack intermediate-scale bedforms of either TARs or megaripples. Both locals show widely-separated dome or barchan dunes, with low sand supply conditions, and driven by broadly uni-directional winds. (a) Chasma Boreale (dune field 0010+846). (b) Olympia Cavi (dune field 0964+804). Notice the order of magnitude larger dune sizes of (a).

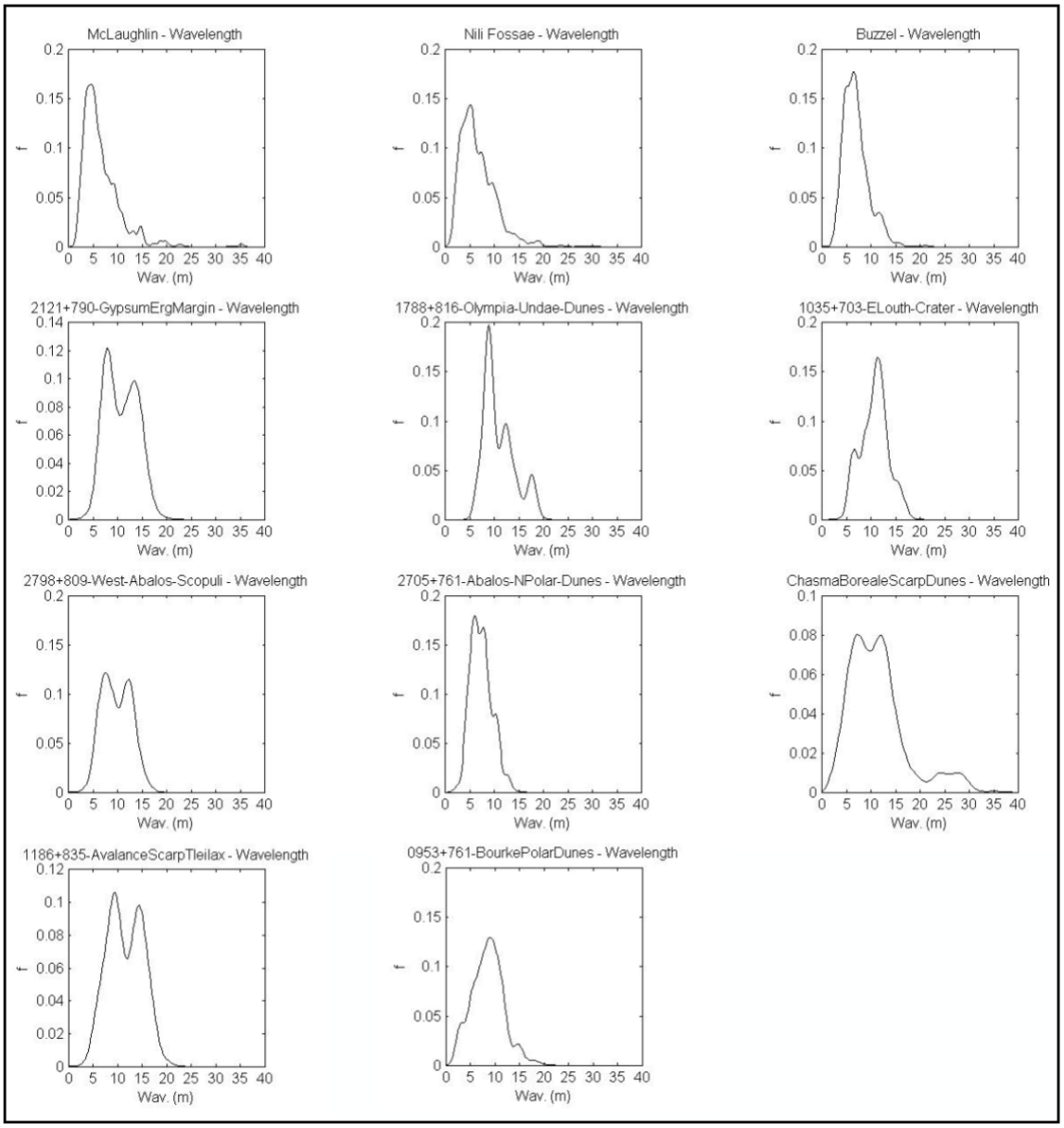

Figure S2. Histograms of active polar megaripple wavelengths from the manual mapping of crest lines. For comparison the top left and center plots are from McLaughlin/Nili Fossae (Silvestro et al., 2020). Compare with Fig 5.

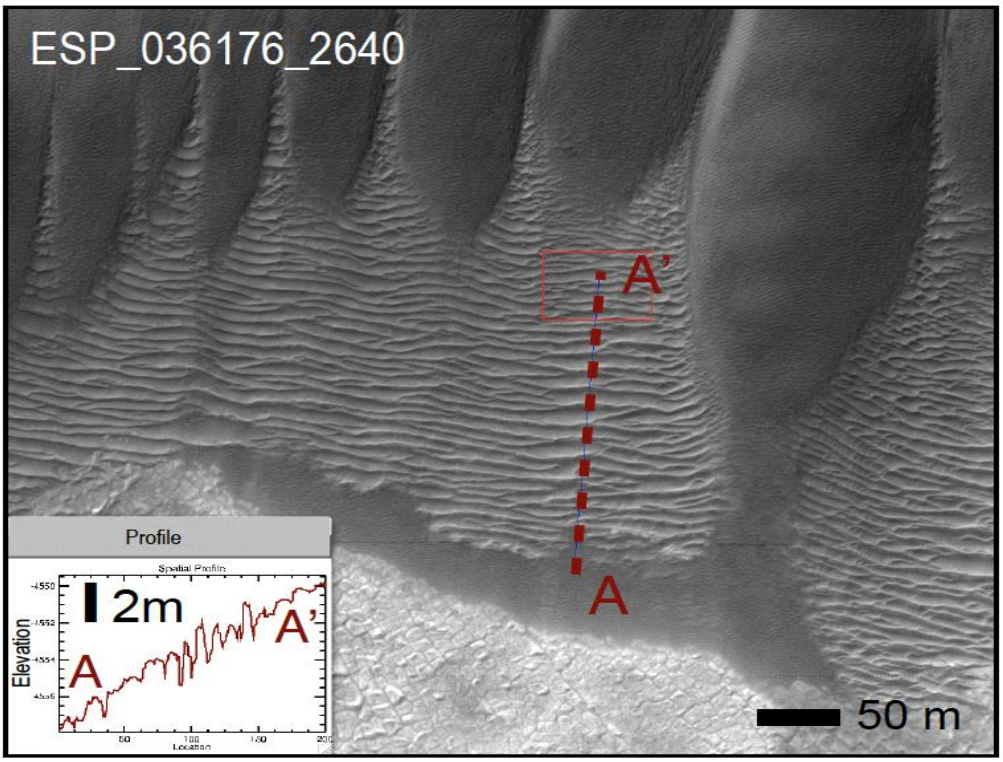

Figure S3. Example of north polar erg active megaripples where bedform heights of 1-2 m are measurable in HiRISE DTMs (1 m/post). Buzzel dune field in the Olympia Cavi reentrant.

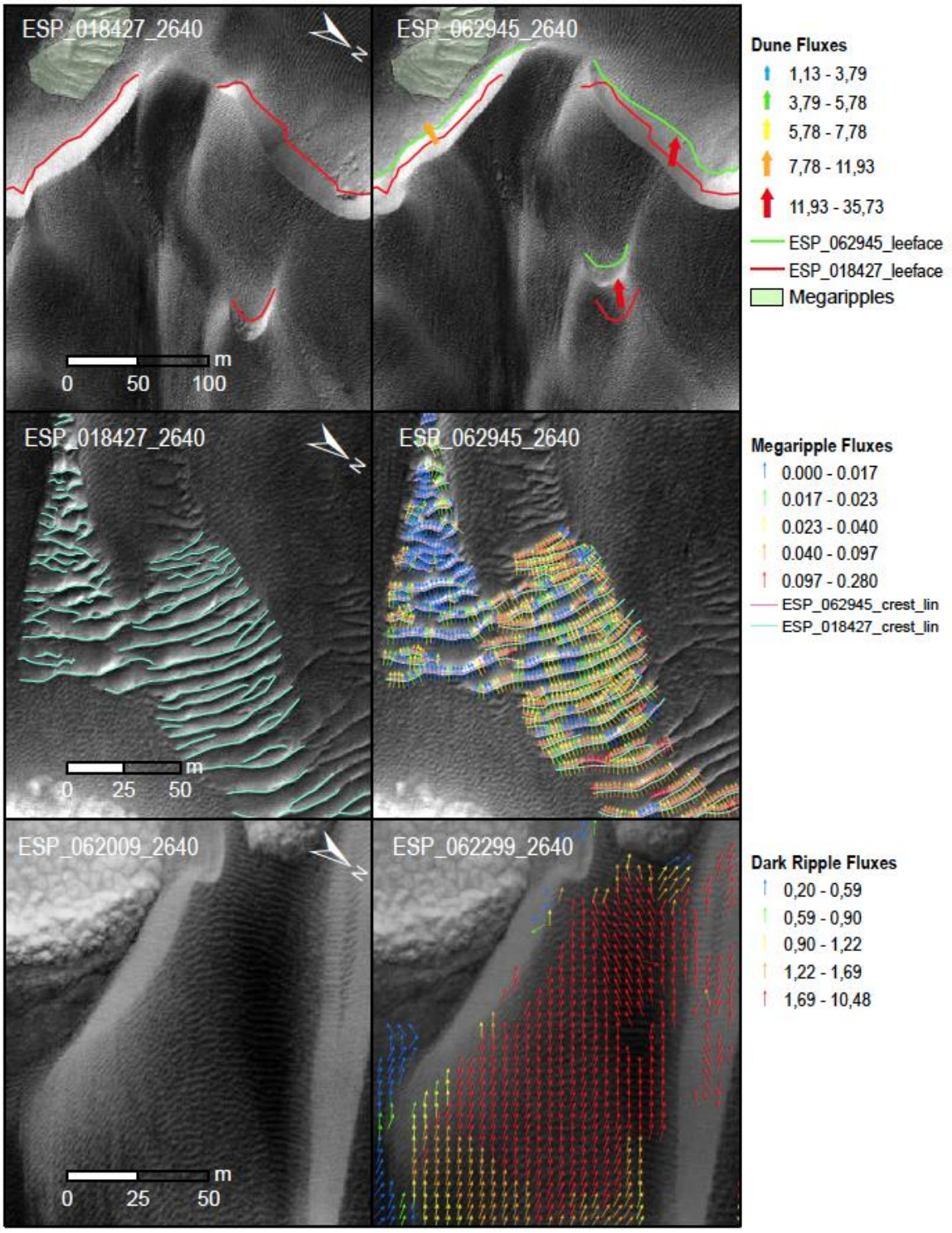

Figure S4. Examples of Buzzel bedforms measurements and activity, with (top) dune crest advancements, (middle) manually-mapped megaripple crest lines, and (bottom) ripple migration during the early summer. All comparisons show the two time periods for the same area and the right subfigures provide flux information. Compare with Fig 7. North is up in all figures.

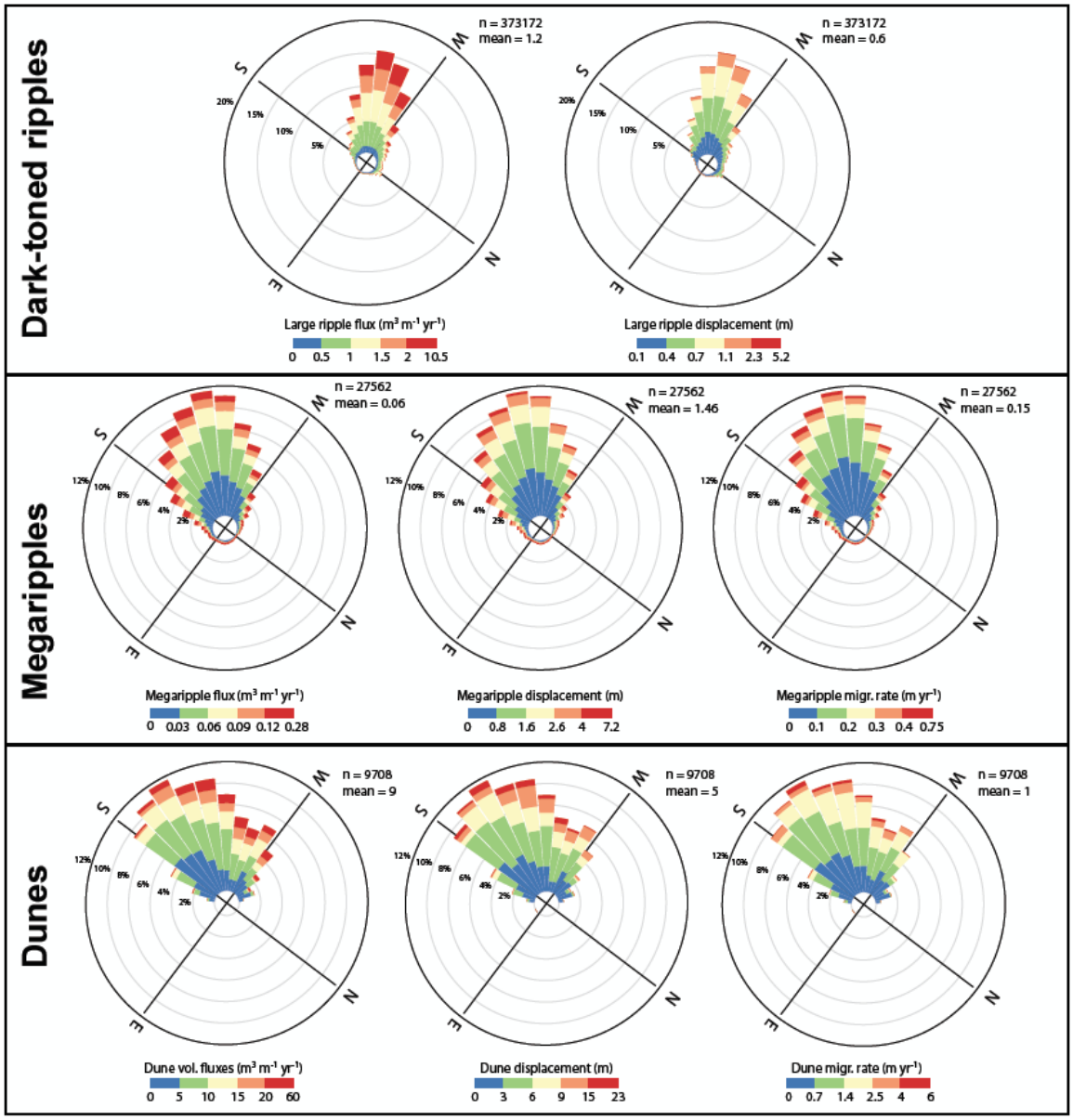

Figure S5. Circular plots showing the distribution of the Buzzel dune field DTR, megaripple, and dune (left) sand fluxes, (center) displacement, and (right) migration rate vectors. Note, ripple migration rate plot is not provided. Compare with Fig 7d.

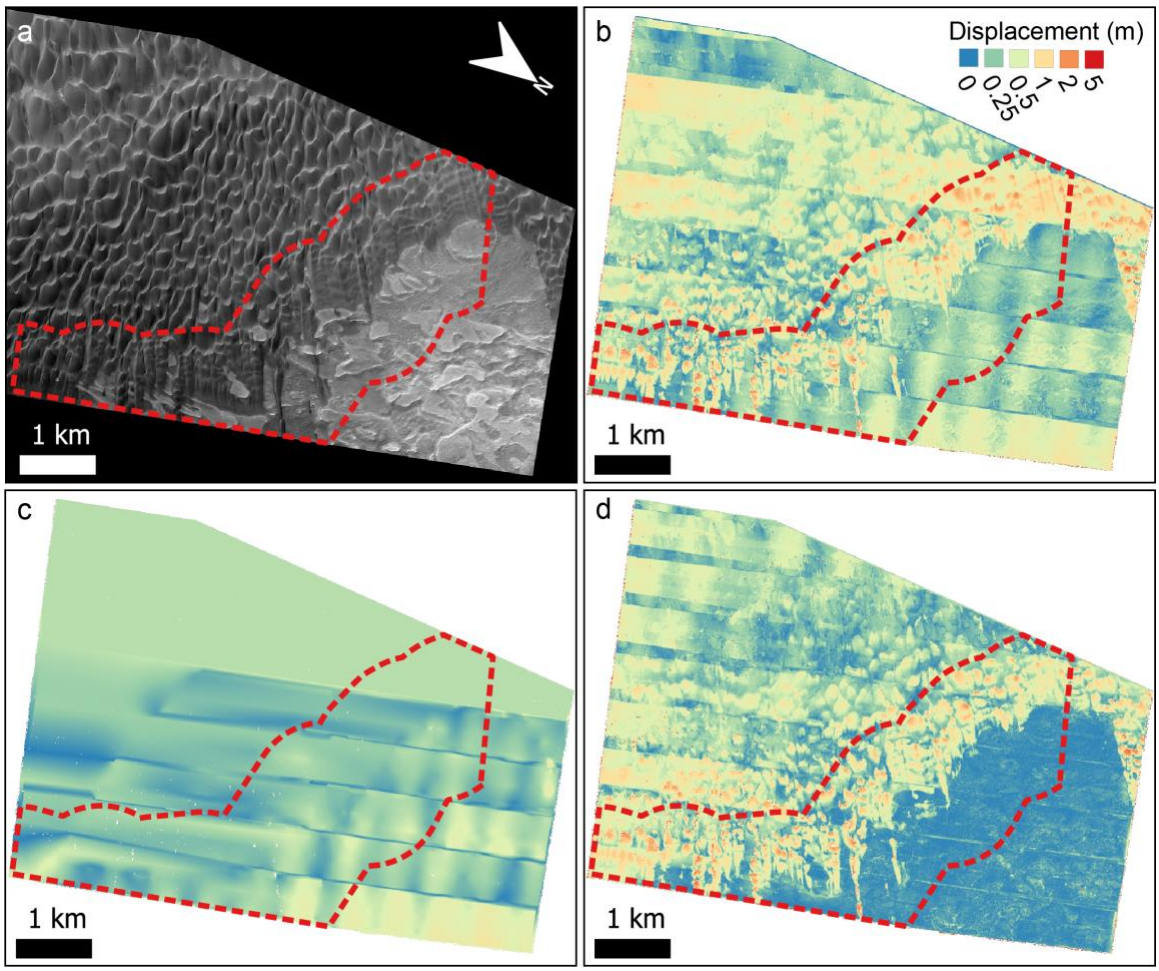

Figure S6. Example of the COSI-Corr correction that was applied to improve the bedform migration rates estimates. The red outline marks the buffer area where the fluxes of the different bedforms where compared. (a) HiRISE orthoimage ESP_062009_2640. (b) COSI-Corr displacement map used to monitor DTRs migration. Note the ~EW bands and long-wavelength wavy pattern caused by CCD misalignments and jitter. This pattern is more obvious in the bedrock areas where displacements should be null. (c) Residual displacements computed using the filtered EW and NS components (refer to Silvestro, et al. 2020 for details); the residuals are computed and extrapolated from the bedrock areas, resulting in a less effective correction with increasing distance from the dune edge. (d) The corrected displacement map; note the improvements in the dune edge, while strong banding is still visible in the southern (left) inner section of the dune field.

Supplemental Tables

Table S1. Objectives 1&2 survey results of north polar dune field morphology and activity[a].

Site name & ID	Survey status (Obj. 1)	Activity status (Obj. 2)	T1 and T2 Images and timing	Duration (Mars years)	Megaripple (MR) activity notes
Chasma Boreale Scarp Dunes - 3393+850	MR	significant megaripple migration/change	PSP_001374_2650 @Ls134 (2006) - ESP_054013_2650 @Ls124 (2018)	6.0	Many stoss and interdune MR migration. Most active MR in high sand volume fields but some on bedrock. Other static MRs in troughs or on stoss-side in the N (maybe frozen crests and/or limited upwind sand supply).
Kolhar Dunes in Chasma Boreale - 0010+846	Neither	no MRs/TARs	PSP_008968_2650 @Ls90 (2008) - ESP_063323_2650 @Ls143 (2020)	6.1	Lack of MR anywhere. Barchan and barchanoid megadunes migrating.
Buzzel Dunes and Polar Scarp - 2329+840	Both	significant megaripple migration/change	PSP_009105_2640 @Ls95 (2008) - ESP_062009_2640 @Ls94 (2019)	6.0	Most stoss leading edge MR moving; some motionless in deep troughs. Most MR in high sand volume fields but some on bedrock migrating.
Tleilax Dunes and Polar Basal Unit - 1188+834	MR	significant megaripple migration/change	PSP_001712_2635 @Ls147 (2006) - ESP_053270_2635 @Ls98 (2017)	6.2	Multiple groups of interdune MR migrating. Few stoss or cliff areas with MRs. Some motionless in deep troughs. Most MR in high sand volume fields.
Chasma Boreale Mega Dunes - 3155+826	MR	significant megaripple migration/change	ESP_027589_2630 @Ls125 (2012) - ESP_063351_2630 @Ls144 (2020)	4.2	Isolated clusters of interdune MR migrating. Truncated with short lengths. Underlying aeolian strata has static crescentic ridges.
Olympia Undae Erg Dunes - 1786+816	MR	limited migration/clear modification	ESP_019023_2620 @Ls134 (2010) - ESP_062631_2620 @Ls117 (2019)	3.9	Isolated groups of interdune MR migrating. Some motionless in deep troughs.

West Abalos Scopuli scarp layers - 2797+808	MR	significant megaripple migration/change	PSP_009433_2610 @Ls106 (2008) - ESP_062034_2610 @Ls96 (2019)	6.0	Swift DTRs near active source scarp. Upwind MR static except inter-crest sand. Upwind barchans with stoss-side migrating MRs. Static deep trough MRs.
Planum Boreum Olympia Undae dunes - 0964+804	Neither	no MRs/TARs	PSP_010020_2605 @Ls127 (2008) - ESP_062937_2605 @Ls128 (2019)	6.0	Lack of MR anywhere. Dome and barchan dunes migrating.
Polar gypsum erg margin changes - 2121+790	MR	significant megaripple migration/change	PSP_009396_2590 @Ls105 (2008) - ESP_044973_2590 @Ls116 (2016)	6.0	Skinny, bright MRs migrating on stoss side of dune and interdune MR trains. Some flank modification of MRs or static deep trough MRs.
Scandia Cavi edge linear dunes - 2094+780	MR	significant megaripple migration/change	PSP_009739_2580 @Ls117 (2008) - ESP_062551_2580 @Ls114 (2019)	6.0	Skinny, bright MRs migrating in trains on flanks of linear dunes. Other clusters of dark MR on stoss sides of dunes.
Abalos Undae Polar crater dunes - 2705+762	MR	significant megaripple migration/change	PSP_009394_2565 @Ls105 (2008) - ESP_062351_2565 @Ls107(2019)	6.0	Widespread active MRs in various contexts (extra- and intra-crater): edges of field, stoss and less sides of barchanoid, and sandsheets on steep crater walls. Isolated and as fields.
Palma (Bourke) Polar Dunes - 0953+761	MR	significant megaripple migration/change	PSP_009743_2565 @Ls117 (2008) - ESP_053469_2565 @Ls105(2017)	5.0	Clear MR migration. Mostly on stoss-side of barchanoid-pairs, none on barchans/domes. Many bright-toned MRs.
East Louth crater - 1035+703	MR	significant megaripple migration/change	PSP_001700_2505 @Ls146 (2006) - ESP_062265_2505 @Ls104 (2019)	6.9	Major changes in MR near dark dunes. Large MR. Mostly transverse motion, but some oblique. Some displacement

	on frosted MR in PSP. Less on edges of small DF.

[a]See Table 1, Fig. 2, 5 & S2 for quantitative details.

Table S2. Survey results for megaripples and TARs using HiRISE (Objective 1)[a].

Bedform class	Megaripples	TARs	Both	Neither
North Polar - 67 aeolian sites (65°N – 85°N)				
Count	59	6	6	8
Perc.	88.1%	9.0%	9.0%	11.9%
Global - 238 aeolian sites (73°S – 85°N)[b]				
Count	184	125	98	27
Perc.	77.3%	52.5%	41.2%	11.3%

[a]Also see Fig. 2 & 4.

[b]See Chojnacki et al. (2021).

Animation Captions:

Animations also available at:
https://www.dropbox.com/sh/ikzgayvdt1m9lsw/AAAZO_E3gLwY_MP7gtyOOXe7a?dl=0

Animation S1. S1_HighFluxBuzzel_animated_RED_018427-062945_2640_ULX30000_ULY26115.gif High flux dune field termed Buzzel below a NPLD scarp and sand source. Megaripples migration occurs on bedrock (lower left) and on the flank areas of proto dunes or barchans. The larger megaripple fields, while partially static, shows certain bifurcating crests that displace. Megaripples are spaced at 5-15 m. Dune field 2329+840.

Animation S2. S2_animated_RED_001374-054013_2650_ULX19621_ULY37886_b.gif Chasma Boreale scarp dunes with active megaripples (white arrows) which are more "typical" in morphology along with larger diagonal and crescentic ripples (black arrows) that show some interesting behavior. Also some long baseline slip face calving events. Dune field 3393+850.

Animation S3. S3_BedrockBuzzel.gif Megaripples migration occurs on bedrock (lower left) and on the flank areas of proto dunes or barchans. The larger megaripple fields, while partially static, shows certain bifurcating crests that displace. Megaripples are spaced at 5-15 m. Dune field 2329+840.

Animation S4. S4_animated_RED_009739-062551_2580_ULX37237_ULY34682.gif Relatively thin, bright megaripples in Scandia Cavi. Active (white arrows) and static (black) megaripples are located here. Dune field 2095+780.

Animation S5. S5_2798+809_West_Abalos_Scopuli_Untitled_009433_053805_2610.gif

An animated time-step sequence of megaripple fields as the stoss end of a west Abalos Scopuli dune field. Active (white arrows) and static (left part of sequence) megaripples are located here. Dune field 2798+809.

Animation S6. S4_BurriedBuzzel_animated_RED_009105-062299_2640_ULX59967_ULY21071_b.gif Another part of the Buzzel dune field using multiple Mars years of observations where scattered groups of megaripples are migrating. Several groups can be found overtaken and buried by ripples, sand sheets or dunes. See Animation S7 for a closer view. Note some pixel quantization occurred during image contrast matching.

Animation S7. S7_LPSC_BurriedBuzzel.gif A closer view of Buzzel dunes and sand sheets that bury megaripples over 6 Mars years. Other megaripples form or are exposed as swifter bedforms pass downwind. Scene is ~260-m-wide. See S6 for context.

Animation S8. S8_animated_RED_001374-054013_2650_ULX6528_ULY29751_b.gif Same dune field as in S2 where there are active megaripples (white arrows) along with the more frequent, brighter, long-wavelength (5-30 m) megaripple or polar TARs (black arrows) that are largely static. Note the sand pathways of proto-dunes migrating right-to-left atop of these degraded bedforms seemingly without effect (bottom two white arrows) and they are hinting that they are partially ice-cemented.

Animation S9. S9_animated_3MY_Buzzel_C.gif An animated three time-step sequence of the Buzzel dune field using 1-m/pixel orthos providing a wide-field of view. Images are spanning 3.8 and 5.7 EY. Note the upwind swift duneforms as compared with the slower barchans and megaripples. Also see Fig. 6c.

References:

Bridges, N.T. et al., 2011, Planet-wide sand motion on Mars: Geology, v. 40, p. 31–34, doi:10.1130/G32373.1.

Chojnacki, M., Banks, M.E., Fenton, L.K., and Urso, A.C., 2019, Boundary condition controls on the high-sand-flux regions of Mars: Geology, doi:10.1130/G45793.1.

Chojnacki, M., Banks, M., and Urso, A., 2018, Wind-Driven Erosion and Exposure Potential at Mars 2020 Rover Candidate-Landing Sites: Journal of Geophysical Research: Planets, v. 123, p. 468–488, doi:10.1002/2017JE005460.

Chojnacki, M., Urso, A.C., Fenton, L.K., and Michaels, T.I., 2017, Aeolian dune sediment flux heterogeneity in Meridiani Planum, Mars: Aeolian Research, v. 26, p. 73–88, doi:10.1016/j.aeolia.2016.07.004.

Chojnacki, M., Vaz, D.A., Silvestro, S., and Silva, D.C.A., 2021, Global Heterogeneity of

Martian Megaripples and Transverse Aeolian Ridges: Distribution and Activity, *in* 52nd Lunar and Planetary Science Conference, Houston, Lunar and Planetary Institute, p. Abstract #2524, http://www.lpi.usra.edu/meetings/lpsc2021/pdf/2524.pdf.

Davis, J.M., Grindrod, P.M., Boazman, S.J., Vermeesch, P., and Baird, T., 2020, Quantified Aeolian Dune Changes on Mars Derived From Repeat Context Camera Images: Earth and Space Science, v. 7, doi:10.1029/2019EA000874.

Kirk, R.L. et al., 2008, Ultrahigh resolution topographic mapping of Mars with MRO HiRISE stereo images: Meter-scale slopes of candidate Phoenix landing sites: Journal of Geophysical Research, v. 113, doi:10.1029/2007JE003000.

Kirk, R.L., Howington-Kraus, E., Redding, B., Galuszka, D., Hare, T.M., Archinal, B.A., Soderblom, L.A., and Barrett, J.M., 2003, High-resolution topomapping of candidate MER landing sites with Mars Orbiter Camera narrow-angle images: MER CANDIDATE LANDING SITE TOPOMAPPING: Journal of Geophysical Research: Planets, v. 108, doi:10.1029/2003JE002131.

Mattson, S., Bridges, N.T., Kirk, R.L., Howington-Kraus, E., Mogk, N., and Ojha, L., 2012, Studying Martian Dune Changes with HiRISE DTMs and Orthoimages, *in* Houston, Lunar and Planetary Institute, p. Abstract #7030, http://www.lpi.usra.edu/meetings/dunes2012/pdf/7030.pdf.

Ould Ahmedou, D., Ould Mahfoudh, A., Dupont, P., Ould El Moctar, A., Valance, A., and Rasmussen, K.R., 2007, Barchan dune mobility in Mauritania related to dune and interdune sand fluxes: Journal of Geophysical Research: Earth Surface, v. 112, p. F02016, doi:10.1029/2006JF000500.

Piqueux, S., Byrne, S., Kieffer, H.H., Titus, T.N., and Hansen, C.J., 2015, Enumeration of Mars years and seasons since the beginning of telescopic exploration: Dynamic Mars, v. 251, p. 332–338, doi:10.1016/j.icarus.2014.12.014.

Runyon, K.D., Bridges, N.T., Ayoub, F., Newman, C.E., and Quade, J.J., 2017, An integrated model for dune morphology and sand fluxes on Mars: Earth and Planetary Science Letters, v. 457, p. 204–212, doi:10.1016/j.epsl.2016.09.054.

Silvestro, S., Chojnacki, M., Vaz, D.A., Cardinale, M., Yizhaq, H., and Esposito, F., 2020, Megaripple Migration on Mars: Journal of Geophysical Research: Planets, doi:10.1029/2020JE006446.

Smith, D.E. et al., 2001, Mars Orbiter Laser Altimeter: Experiment summary after the first year of global mapping of Mars: J. Geophys. Res., v. 106, p. 23689–23722, doi:10.1029/2000JE001364.

Sutton, S., Chojnacki, M., Kilgallon, A., and Team, H., 2015, Precision and Accuracy of Simultaneously Collected HiRISE Digital Terrain Models, *in* 46th Lunar and Planetary Science Conference, Houston, Lunar and Planetary Institute, p. Abstract

#3010, http://www.lpi.usra.edu/meetings/lpsc2015/pdf/3010.pdf.

Urso, A., Chojnacki, M., and Vaz, D.A., 2018, Dune-Yardang Interactions in Becquerel Crater, Mars: Dune-Yardang Interactions in Becquerel Crater, Mars: Journal of Geophysical Research: Planets, doi:10.1002/2017JE005465.